Mist Flow in Through-Tool Minimum Quantity Lubrication Drilling: Two-Phase Flow Simulation and Experimental Observation

Jay K. Raval
J. Mike Walker '66 Department of Mechanical Engineering,
Texas A&M University,
College Station, TX 77843
e-mail: jkraval@tamu.edu

Bruce L. Tai[1]
J. Mike Walker '66 Department of Mechanical Engineering,
Texas A&M University,
College Station, TX 77843
e-mail: btai@tamu.edu

Through-tool minimum quantity lubrication (MQL) drilling has been used in industry for decades, but little information is available on the coolant channel design and the effect on fluid distribution due to the inability of in-situ measurement. This study utilizes an Euler–Lagrange computational fluid dynamics (CFD) model to uncover the two-phase flow behavior in MQL drilling. Air is the primary phase modeled as a compressible and turbulent flow. The lubricant droplets are simulated as discrete particles with a proper size distribution. Two-way coupling and droplet-wall interactions are both considered. The results show that the primary phase can reach velocities in the transonic region and is dependent on the helical path of the channel. In addition, most of the lubricant droplets (>95%) impact the channel wall to form fluid film instead of following the air stream. In the cutting zone, droplets can hardly reach the cutting edges in both circular and triangular channel shapes. Finally, a custom-made drilling testbed, along with a transparent work-material simulant, is used to observe and qualitatively validate these results.
[DOI: 10.1115/1.4056146]

Keywords: MQL, Euler–Lagrange model, discrete phase model, drilling, through-tool coolant, in-situ flow visualization, machining processes, modeling and simulation

1 Introduction

Drilling is the most common process in high-volume automobile and aerospace part manufacturing [1]. More and more manufacturers are adopting minimum quantity lubrication (MQL) in machining due to its cost and environmental benefits [2]. As the name implies, MQL is based on utilizing the minimum amount of lubricant required for the process. An aerosol of the lubricant is created using pressurized air and supplied to the cutting zone. This reduces the total lubricant consumption, and moreover, the parts produced are free of cutting fluid residue and ready for the next process [3]. In deep-hole drilling operations, since the cutting zone is not easily accessible with an external MQL supply, the use of internal through-tool channels is necessary. These through-tool channels are common in the production drill bits to deliver cutting fluid. However, unlike flood cooling, the quantity of lubricant used in MQL is typically less than 100 ml/h, which is the order of magnitude lower. It is critical to optimize the delivery of the lubricant to achieve maximum benefits. A prior study by the authors has shown that the drilling performance did not necessarily increase with the amount of MQL flowrate in these through-tool channels [4].

The exit of the through-tool channels is typically on the flank face of the tool, and therefore, not all the fluid can penetrate into and evenly distribute in the cutting zone. Experimental studies on externally applied MQL have shown that the location of fluid application and tool geometry are influential parameters of the cutting performance [5,6]. It is not hard to imagine the same impacts on the cutting edges of a drill bit. However, it is technically challenging to experimentally evaluate these variables since there is no optical access to the cutting zone to visualize the flow of the cutting fluid in drilling. Multiple studies have characterized MQL machining, but these studies were limited to the flow only at the exit of the channels and focused on droplet diameter distribution, flow velocity, and mass flowrate rather than the coverage of oil droplets [7,8]. Therefore, this study aimed to visualize MQL flow in the through-tool MQL drilling scenario. Specifically, the objective is to develop a computational fluid dynamics (CFD) model adopted from sub-models developed for other applications to simulate droplet trajectories with different internal channel designs. The results are validated experimentally using a flow visualization technique developed by the authors.

Multiple research teams have performed studies on numerically modeling the MQL flow for open configurations such as turning and milling, but very little work has been found on through-tool drilling [9,10]. The through-tool channels in a drill bit follow the helical flutes. The flow of fluid in a helical channel is known as Dean flow and is characterized by the Dean number [11]. Dean studied the flow of an incompressible fluid in a toroidal pipe and showed the effect of curvature on the flow contours. Later, Germano and Yamamoto et al. extended Dean's work into helical channels and showed that the secondary flow pattern changes based on the torsion and curvature of the helix [12–14]. Based on that, multiple authors have performed CFD for through-tool drilling for flood cooling operations but not for MQL [15,16]. In a very recent paper, Falcone et al. modeled the MQL flow in a circular through-tool channel using an Euler–Lagrange–Euler model [17]. Their work was focused on the formation of the fluid film on the through-tool channel and the deposition of the droplets on the channel. However, no discussion was provided about the principles behind the distribution, and the flow of the droplets near the cutting edge was not modeled.

Many models are available for multi-scale modeling based on different applications [18]. Since MQL is a multiphase flow, the

[1]Corresponding author.

Manuscript received June 9, 2022; final manuscript received October 29, 2022; published online November 30, 2022. Assoc. Editor: Karl R. Haapala.

ideal method of simulation is the Eulerian two-phase approach, such as volume of fluid (VOF). However, the mesh requirements for the VOF method require the mesh to be smaller than the size of the droplets of the secondary phase. Droplets as small as 0.5 μm have been measured by researchers for MQL flow [19–21]. Also, the through-tool channel length can range anywhere between 50 mm and 300 mm, with a diameter ranging from 0.7 mm to 2 mm. Therefore, for using VOF, elements as small as 0.25 μm are needed for a control volume, which is a few orders of magnitude smaller for the length scale of the model. This makes the use of VOF method to simulate MQL flow computationally expensive and inefficient. For this reason, this study adopted a Lagrangian-based droplet tracking approach, namely discrete phase model (DPM) [22]. The lubricant flowrate in MQL ranges from 5 ml/h to 300 ml/h, while the air flowrate ranges from 50 l/min to 300 l/min [23]. Therefore, the secondary phase volumetric flowrate is only about 1–2% of the primary phase. Since the Lagrangian approach can provide good accuracy for volume fractions up to 12%, it is suitable for the current application. Therefore, an Euler–Lagrange coupled approach was adopted here using the FLUENT® module of ANSYS (Canonsburg, PA). The primary phase was modeled as a continuum through the Euler formulation, while the secondary phase (i.e., droplets) was modeled using the Lagrangian approach. This paper also applied the model in the cutting region with different through-tool channel shapes (circular and triangular) and with a common drill tip groove called "gash".

For model validation, an in-situ visualization of drilling is difficult due to the lack of optical access to the drilling zone. Post-analyses on tool wear also cannot provide direct evidence of lubricant penetration and distribution. Few methods have been proposed to characterize and observe the flow effect directly. For example, John coated the drill with a proprietary polymer coating and looked at the wear of the coating to correlate the fluid flow velocities with it [24]. However, this method does not involve actual cutting of the workpiece, and the contact between the cutting edge of the drill and the workpiece is also absent. Another method proposed by Fallenstein and Aurich used a transparent acrylic workpiece with a pre-drilled hole to be able to visualize the fluid flow in the cutting region [25]. This method provides in-situ flow data, but it does not involve the rotation of the drill or active cutting to form chips. Therefore, to better validate the simulation, a new testbed is also presented in this study that involves actual drilling of a clear material, which allows optical access from the bottom of the hole to observe the flow.

This paper is structured as follows. Section 2 includes a brief discussion of different drill geometries, meshing, and material properties of the fluids. Section 3 describes the setup of the CFD model, the details of the sub-models, and the coupling between the control volumes. The created model is then applied to different through-tool channel geometries, and the results for the through-tool channel and the cutting region are shown and analyzed in Sec. 4. Section 5 introduces the in-situ flow visualization technique developed by the authors to replicate critical aspects of through-tool MQL drilling and uses it to validate the CFD results. Section 6 discusses the plausibility of the results and the limitations of the model. Finally, Sec. 6 concludes with important findings from this study.

2 Drilling Tool Geometries and Mesh

A 9.5 mm (3/8 in.) diameter drill with reduced web design and a helix angle of 30 deg was selected for the current study and designed in SolidWorks. This is because most drilling tools have a standard 30 deg helix angle, and high-performance drills often use reduced web with a split point. Figure 1 shows the computer-aided design model of the drill body used for the study. Since circular and triangular channels are both commercially available, drill bits with these channel shapes are modeled. The location and size of the through-tool channels are estimated based on commonly

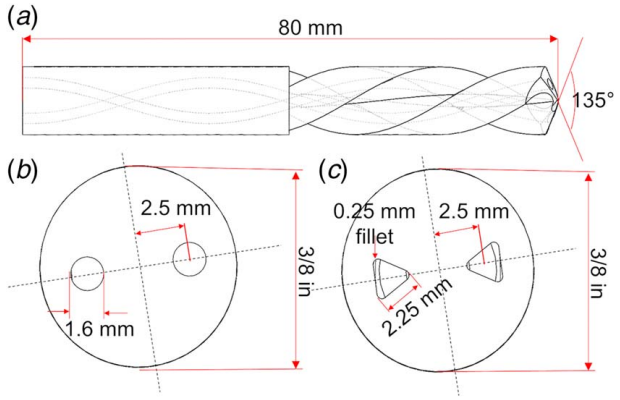

Fig. 1 (*a*) Side view of the drill, (*b*) front view of circular channel drill, and (*c*) front view of triangular channel drill

available drills of a similar size. The circular channel has a diameter of 1.6 mm with a cross-sectional area of 2.01 mm^2, and the triangular channel has a cross-sectional area of 2.06 mm^2. A small fillet of 0.25 mm is added to the corners since sharp corners are not practically possible. In addition, a gash is considered at the drill point. The gash is a secondary cut on the drill flank face, known for its ability to improve fluid flow. A total of four cases are studied to test the CFD model and to investigate the influence of the drill geometry on the distribution of lubricant. The 3D models of these cases are all shown in Fig. 2.

In the model, every drill orientation is vertically placed (along the gravity). Boolean operations are used to generate a negative model of the drill, which represents the control volume of the fluid flow. Figure 3(*a*) shows the complete control volume of the fluid flow, including the through-tool channels, cutting region, and flute. Due to symmetry, only half of the control volume was modeled. Furthermore, to reduce the computational load and also improve the detail of the modeling results at the drill tip, the whole control volume was separated into two sections, the through-tool channel section, and the cutting region section, as shown in Figs. 3(*b*) and 3(*c*), and modeled separately. The partition was performed at 15 mm from

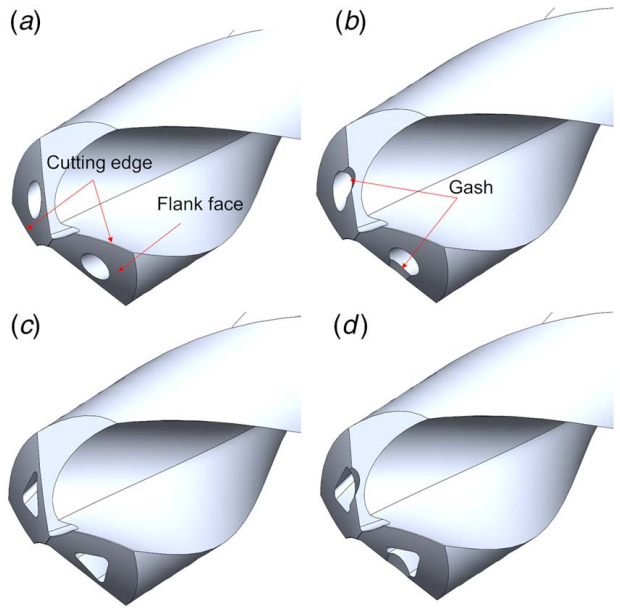

Fig. 2 Isometric view zoomed at the drill point: (*a*) circular channel drill without gash, (*b*) circular channel drill with gash, (*c*) triangular channel drill without gash, and (*d*) triangular channel drill with gash

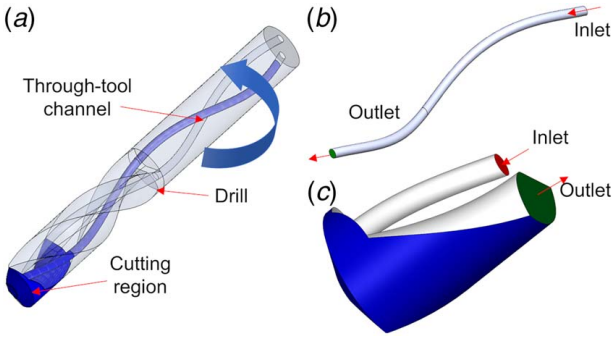

Fig. 3 (*a*) Control volume for the flow as a negative of the drill, (*b*) through-tool channel control volume, and (*c*) cutting region control volume (Color version online.)

the drill tip, about 1.5 times the drill diameter. Since the total control volume was separated into two sections, coupling between the flow from the through-tool channel region to the cutting region control volumes was needed. Details for the coupling of the flow between the two control volumes are given in Sec. 3.3.

Due to the complex geometry of the control volume, an unstructured tetrahedral mesh was used to discretize the control volume. In addition, inflation layers were used to capture the viscous boundary layer near the wall, and mesh refinement was performed until a wall y-star value ranging from 1 to 5 was achieved by using inflation layers. The cross-sectional mesh for the circular and triangular channels is shown in Figs. 4(*a*) and 4(*b*). The mesh size on the channel wall was 0.05 mm, and the thickness of the first inflation layer was 25 μm. The mesh size in the bulk of the volume is 0.15 mm, resulting in a total of about 5 million tetragonal elements for the circular channel and 4.5 million for the triangular channel. An isometric view of the mesh for the cutting region of a circular channel without a gash is shown in Fig. 4(*c*). There were a total of 14 million tetragonal elements in the control volume. The element size in the bulk of the fluid was 0.25 mm, and the element size on the hole bottom and drill flank face were 0.01 mm. Inflation layers were also added to the through-tool channel and flute region of the control volume, as shown in

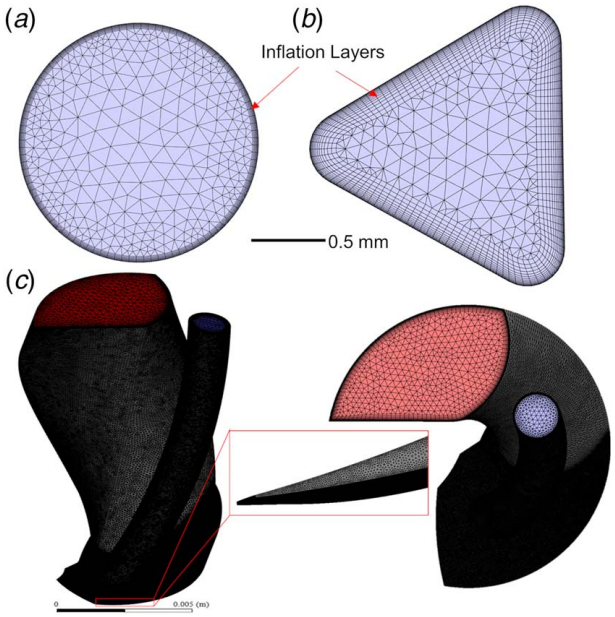

Fig. 4 Images for the mesh: (*a*) circular channel cross-sectional mesh, (*b*) triangular channel cross-sectional mesh, and (*c*) mesh for the cutting region

Table 1 Properties of the fluid used for the study

Property	Air	Lubricant
Density at 300 K, kg/m^3	1.125	835
Viscosity at room temperature, Pa · s	$1.72 * 10^{-5}$	$2.05 * 10^{-2}$
Vaporization temperature, K	N/A	450
Boiling temperature, K	N/A	500
Surface tension, dyn/cm	N/A	30

Fig. 4(*c*), with a close-up image of the mesh near the cutting edge. A grid independence study was performed with a 25% coarser and 10% and 25% finer mesh size. The results showed that the original mesh size is capable of properly discretizing the control volume and capturing all the important aspects of the flow.

Table 1 shows the properties of the primary phase, air, and lubricant used in the study. The values are based on commercially available MQL lubricants [26]. The primary phase air was modeled as a compressible fluid to account for the changes in the density of the fluid and follows the ideal gas equation to relate the pressure, temperature, and density.

3 Computational Fluid Dynamics Model

The numerical model was built in ANSYS FLUENT due to its capacity to model complex phenomena of MQL flow. The axial velocity of the drill is negligible compared to the rotational velocity; therefore, only the rotation of the drill at a constant rpm of 500 is modeled. The flow was modeled in a moving reference frame to ensure that the centrifugal and Coriolis forces were properly modeled. All the walls of the control volume except the hole bottom and hole side walls rotate along with the reference frame (the drill axis); the hole bottom and hole side walls are stationary in the inertial reference frame. These walls are highlighted in blue in Fig. 3(*c*). The no-slip boundary condition was employed at all the walls, and wall surfaces were assumed to be smooth.

Pressure boundary conditions were used at all inlet and outlet sections. To correctly enter the boundary conditions, a calibration test was conducted separately. Drill bits with the exact geometries of Figs. 2(*a*)–2(*c*) were 3D printed using high-resolution (25–50 μm) stereolithography (SLA). Small holes about 0.1 mm were made on the drill body to access the through channels and thus allowed a pressure gauge to measure the static pressure at the required locations. These access holes were small enough not to distort the flow field. The total pressure at the inlet of the through-tool channel region was 60 psi (413 kPa), and the static pressure 15 mm above the drill tip was measured to be 20 psi (138 kPa) for both channel shapes. This value was used as the boundary condition at the outlet of the through-tool channel region (Fig. 3(*b*)) and the inlet of the cutting zone region (Fig. 3(*c*)). Since the fluid exits the control volume into ambient air, the static pressure at the outlet of the cutting region control volume was set as 0 psi (gage). The lubricant droplets were injected normal to the inlet face of the through-tool channel control volume at a velocity of 50 m/s distributed uniformly across the whole area and a volumetric flowrate of 15 ml/h to represent an actual drilling condition. A sensitivity analysis of the effect of the inlet speed and direction of the droplets was performed. The through-tool channel length was long enough for the inlet conditions of the droplets to have no influence on the outlet droplet velocity and location.

The primary phase, air, is modeled using Eulerian equations as a continuum. The secondary phase is modeled using a Lagrangian approach as discrete droplets inside the control volume. DPM is an Euler–Lagrange model and reduces the computational load considerably compared to the Euler–Euler model (i.e., volume of fluid). It models the flow of spherical droplets dispersed throughout the control volume and can be used safely when the volumetric loading of the second phase is less than 10%. The flow field of

the primary phase is solved first, and the generated flow field is used to calculate the path of the lubricant droplets using force balance. The forces include drag force, centrifugal force, Coriolis force, and gravitational force. Section 3.1 describes the details of the model for the primary phase and Sec. 3.2 describes the details for modeling the secondary phase.

3.1 Primary Phase Modeling. The primary phase is modeled as a steady-state compressible flow. The governing equations are the continuity equation (Eq. (1)) and the Navier–Stokes conservation of momentum equation (Eq. (2)). The momentum equations are modified to incorporate the effect of constant rotation. The final form of the governing equations is as follows:

$$\nabla \cdot \rho_a \mathbf{V} = 0 \tag{1}$$

$$\nabla \cdot (\rho_a \mathbf{V}\,\mathbf{V}) + \rho_a(2\boldsymbol{\Omega} \times \mathbf{v}_r + \boldsymbol{\Omega} \times \boldsymbol{\Omega} \times \mathbf{r}) = -\nabla p + \nabla \cdot \bar{\bar{\tau}} + \mathbf{F}_g \tag{2}$$

In the aforementioned equations, $\mathbf{V}$ is the velocity vector, $\boldsymbol{\Omega}$ is the rotation vector, $\boldsymbol{\tau}$ is the stress tensor, $\mathbf{F}_g$ is the gravitational force, and ρ_a is the density of air. The primary phase velocity can reach up to 250 m/s in channels of 1.5 mm diameter based on the reported data [23]. The approximated Reynolds number for the fluid in the through-tool channel is about 25,000, which falls under the turbulent flow regime. Therefore, modeling the turbulent nature of the flow is necessary. The Reynolds averaged Navier–Stokes formulation of the turbulence in the conservation of the momentum equation was used. Two equation turbulence models were used here for their accuracy and low computational load. The k–ω SST model was chosen because of its capacity to shift between the standard k–ω model and the standard k–ε model based on the location. The k–ω model was used in the near-wall region due to its higher accuracy, while the k–ε model was used in the bulk of the flow due to its freestream independence. The k is the kinetic energy of the fluid, ω is the specific rate of dissipation, and ε is the rate of dissipation of kinetic energy. The turbulence intensity at the inlet was set as 5%, a common setting in CFD.

3.2 Secondary Phase Modeling. The flow of the lubricant droplets is modeled using DPM, which is a Lagrangian tracking model. The modeling of the second phase can be transient irrespective of the primary phase being steady-state or transient. The time-step used for calculating the droplet tracks was 10^{-5} s with a total simulation time of 0.005 s. This was selected because the residence time of the droplets was in the order of 10^{-6} s. For each iteration of the primary phase, one time-step of the DPM was evaluated. The parcel approach was used to reduce the computational load. FLUENT combines droplets with similar properties into a parcel and tracks parcels instead of tracking the individual droplets. It can model the interaction of the droplets with the primary phase, amongst themselves as well as the walls. For this study, since the volume flowrate of the lubricant droplets was very low (1–2%) and droplets are small (1–3 μm), droplet-droplet interactions were neglected. Furthermore, droplet breakup and coagulation were not included in the model. Two-way coupling between the droplet and primary phase and the droplet-wall interactions were both considered.

The droplet tracks are calculated using Eq. (3), which is normalized per unit mass. The first term on the right-hand side represents the droplet inertia per unit mass. The first term on the right represents the drag force (F_D) per unit mass generated due to the difference between the velocity of primary flow and droplets [22]. Due to the flow in the transonic range, a modified high Mach number drag coefficient (C_D) based on the work of [27] is used here. It is to be noted that the Reynolds number (Re) in Eq. (3) is based on the difference in the velocity of primary phase velocity (V_i) and the droplet velocity (V_{di}). The effective gravitational force after including the buoyancy effect is given by the second term on the right, where ρ_d is the droplet density and ρ is the air density, and g_i is the gravitational force in ith direction. The last term ($\mathbf{F}$) accounts for the forces due to moving reference frame, i.e., the centrifugal force and the Coriolis force. For a control volume rotating around the Z-axis, the third term on the right side can be separated into the forces in X and Y directions. These equations are shown in Eqs. (4) and (5). The first term on the right-hand side of both Eqs. (4) and (5) is the centrifugal force and the second term is the Coriolis force.

$$\frac{dV_{di}}{dt} = F_D(V_i - V_{di}) + \frac{g_i(\rho_d - \rho_a)}{\rho_d} + F,$$
$$i = x, y, z \;\&\; F_D = \frac{18\,\mu\, C_D\, \mathrm{Re}}{24\,\rho_d\, d_d^2} \tag{3}$$

$$F_x = \left(1 - \frac{\rho}{\rho_d}\right)\Omega^2 x + 2\Omega\left(V_{d,y} - \frac{\rho}{\rho_d}V_y\right) \tag{4}$$

$$F_y = \left(1 - \frac{\rho}{\rho_d}\right)\Omega^2 y + 2\Omega\left(V_{d,x} - \frac{\rho}{\rho_d}V_x\right) \tag{5}$$

To account for the dispersion of the droplets due to turbulence, the discrete random walk (DRW) model was employed. DRW is a stochastic droplet tracking model which includes the effect of local velocity fluctuations on the droplet trajectories. The droplet-wall interactions are modeled using the wall film model, which is based on the work of Stanton and Rutland [28]. This model was employed since the formation of the fluid film on the channel wall is important for MQL flow. This model is valid for fluid films thinner than 500 μm since the simplified linear fluid velocity profile is used inside the fluid film. When a droplet impacts a wall, depending on the energy of the impact, the droplet can either stick to the wall, spread on the wall surface, or splash and form smaller droplets, as shown in Fig. 5. The criterion to determine the outcome is based on the energy of the droplet before the impact. The impact energy ϵ of the droplet can be calculated based on Eq. (6). Apart from the droplet properties, the primary phase boundary layer thickness (δ_{bl}) and the height of the preexistent fluid film (h_o) also influence the outcome. V_d is the velocity of the droplet in the normal direction to the wall and σ is the surface tension of the lubricant. For low energy impact, the droplet sticks to the wall, attains the velocity of the wall, and forms a fluid film. For medium energy impact, the droplet spreads on the wall and its velocity in the tangential direction to the wall is calculated based on the work of Naber and Reitz [29]. For high energy impact, the droplet splashes and forms smaller droplets. For this study, if splashing occurs, the primary droplet gets divided into four smaller droplets whose sizes are calculated empirically using a probability density function based on the work of Mundo et al. [30]. The mass fraction splashing from the surface (y_s) is based on an empirical relationship developed by Mundo et al. and is

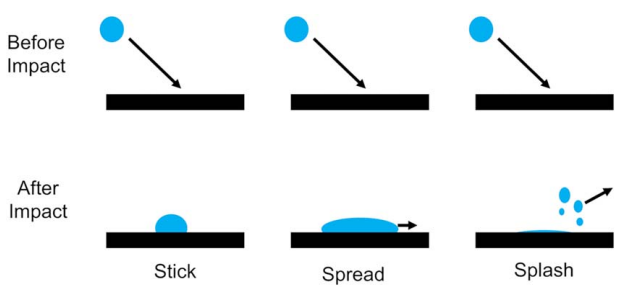

Fig. 5 Droplet-wall interaction outcomes

shown in Eq. (7) [30].

$$E = \sqrt{\frac{\rho_d V_n d_d}{\sigma}\left(\frac{1}{\min\left(\frac{h_0}{d_d}, 1\right) + \frac{\delta_{bl}}{d_d}}\right)} \tag{6}$$

$$y_s = \begin{cases} 1.8 * 10^{-4}\left(E^2 - E_{crit}^2\right) & , \ 57.7 < E < 86.6 \\ 0.70 & , \ E > 86.6 \end{cases} \tag{7}$$

Multiple researchers have measured and reported the droplet size at the exit of MQL tools. The average droplet size ranges from 0.5 μm to 10 μm depending on the MQL system and cutting tool used [19,31]. Based on the results published by Dasch and Kurgin, the greatest number of droplets falls in the range of 1–1.5 μm for a dual-channel internal MQL system [32]. However, it is to be noted that these sizes are measured at the exit of the cutting tool, and secondary atomization can occur as the droplets exit the through-tool channel. Therefore, these measurements may not accurately represent the droplet sizes inside the through-tool channel. For this study, a Rosin–Rammler droplet distribution with a minimum droplet diameter of 1 μm, a maximum diameter of 3 μm, and a mean diameter of 1.5 μm was assumed. The histogram in Fig. 6 shows the fraction of total mass carried by the particular size droplets. Larger droplets (>3 μm) were avoided from the simulation because they have a high Stokes number (over 10). For such high values of Stokes number, the droplet momentum dominates the path of the droplets, and therefore, do not follow the primary flow and end up sticking to the wall as a fluid film on the channel wall. Also, since droplet-droplet interactions are not included in the model, they never move inside the fluid film. Therefore, the focus of the study is limited to smaller droplets that have low particle residence time and are expected to follow along with the primary phase and penetrate deeper into the cutting zone.

3.3 Transfer of Flow Between the Control Volumes. Since the whole control volume was separated into two smaller sections to facilitate finer mesh with the same resources, coupling the flow from the outlet of the through-tool channel control volume and the inlet of the cutting region control volume is needed. For the primary phase, the velocity distribution, static pressure, and total temperature obtained at the outlet of the through-tool channel region after the solution has converged are saved as a profile file. This profile file is used as the inlet boundary condition for the cutting region. This ensures that the fluid profile developed due to the geometry of the through-tool channel gets transferred to the cutting region and reduces the number of iterations required for the numerical solution in the cutting region to converge. For the secondary flow, a monitor is set at the outlet of the through-tool channel region, which captures the exit location, velocity, temperature, mass, and time of the droplets crossing the boundary and reports it into a text file. This text file is used to set the droplet injections for the cutting region control volume. This approach helps decouple a large control volume into smaller regions. However, there can be continuity issues with this approach if the boundary conditions are ill-posed and might lead to divergence. Also, if the droplets present zero velocity, for example, being stuck on the wall as fluid film, they are not recorded as the input, which leads to a continuity issue.

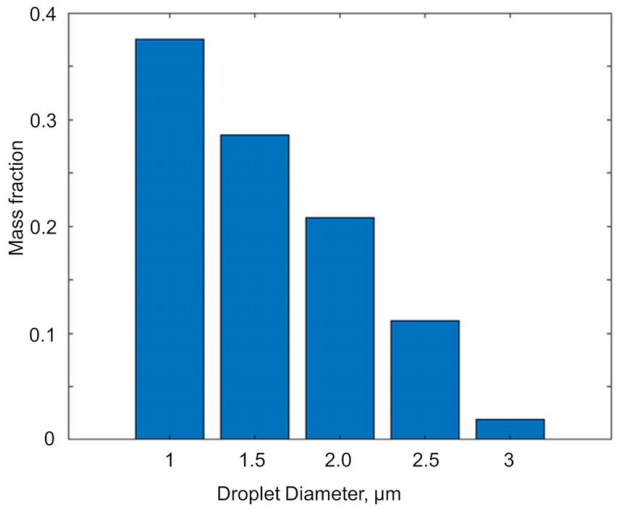

Fig. 6 Bar plot of mass distribution between droplet sizes

4 Numerical Results and Analysis

The velocity streamlines of the primary phase, the volume fraction of the secondary phase, and the lubricant film thickness are analyzed to identify the differences between the cases. These results are also discussed and compared with available literature data for their correctness.

4.1 Through-Tool Channel Region

4.1.1 Primary Phase. The channel shape has a great influence on velocity distribution and, therefore, can affect the lubricant distribution. Figure 7(*a*) shows the exit axial velocity contours for the circular channel. The axis of rotation is on the left side of the cross section. It can be clearly seen that the velocity is not uniform across the cross section and differs from the flow profile of turbulent flow in a circular channel. The maximum velocity region is shifted radially outwards and toward the bottom side of the channel. Similarly, for the triangular channel, the maximum velocity region is shifted radially outwards with higher velocities near the corners, as shown in Fig. 7(*b*). This type of velocity profile is observed due to the secondary flow generated in the fluid. The helical path of the channel and the rotation of the drill generate centrifugal force and Coriolis force. The centrifugal force moves the fluid radially outwards, while the Coriolis force moves the fluid toward the bottom side of the image shown. The axis of rotation is on the left side of the image coming out of the plane, and the direction of rotation is clockwise.

The average velocity at the outlet for the circular channel is 286 m/s. The average exit velocity for the triangular channel is 260 m/s which is slightly lower than that of the circular channel. In the through-tool channel region, the average velocity at the outlet for the circular channel, as shown in Fig. 7(*a*), matches well with the average velocity measured by Stephenson et al. [23]. Although no published data for the average velocity at the outlet of a triangular channel is available, the value obtained from the CFD results is found reasonable. Although the cross section area is 2.5% larger, the hydraulic diameter of the triangular

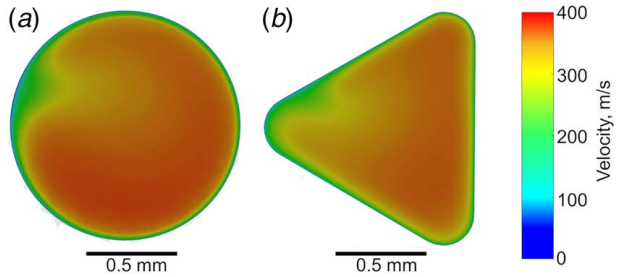

Fig. 7 Primary phase velocity streamlines for the through-tool channel region: (*a*) circular channel and (*b*) triangular channel

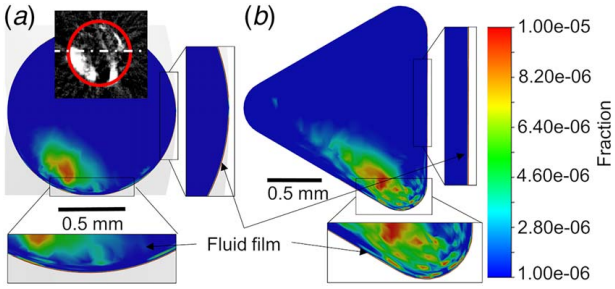

Fig. 8 Lubricant volume fraction at the outlet: (*a*) circular channel and (*b*) triangular channel

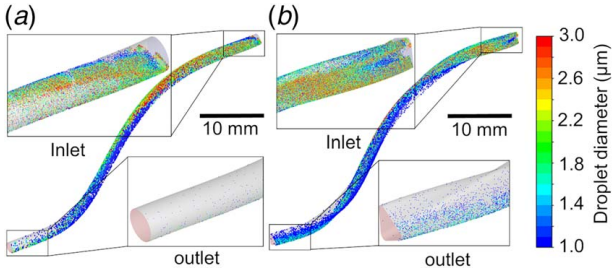

Fig. 9 Droplet location based on their size: (*a*) circular channel and (*b*) triangular channel (Color version online.)

channel is 23% smaller. This reduction in the hydraulic diameter increases the pressure drop, and therefore a lower outlet velocity is expected. This is also supported by the average total pressure at the channel outlets. The total pressure at the outlet for the circular channel is 46.1 psi (318 kPa) while that for the triangular channel is 42.8 psi (296 kPa).

4.1.2 Secondary Phase. The lubricant concentration at the exit of the circular and triangular channels is shown in Figs. 8(*a*) and 8(*b*), respectively. It can be clearly seen that the lubricant does not distribute uniformly across the area. For the circular channel, a higher droplet concentration is obtained at the bottom left corner of the channel cross section. Most droplets end up sticking to the channel wall and form a fluid film on the wall, as shown in the zoomed images. The formation of this fluid film is only on the bottom and right sides of the channel; the top region does not have any fluid layer formed. The experimentally measured lubricant distribution in a previous work by authors is also shown in Fig. 8(*a*). The white region represents the presence of lubricant and the black region represents the absence of lubricant. The general location of the distribution of the droplets matches with the results experimentally measured and reported by the authors' prior work [33]. The experimental results also show that most droplets exit closer to the axis, which is on the left side of the image shown in Fig. 8(*a*). For the triangular channel, a large quantity of lubricant is seen near the bottom corner and some near the left corner. Most of the droplets exit near the bottom corner of the channel, as shown in Fig. 8(*b*). The fluid film formation on the wall starts from the mid portion of the bottom wall and extends up to the top corner.

Figure 9 shows the instantaneous droplet location in the through-tool channel. The droplets are colored based on their diameter. As can be seen from the zoomed images of the inlet, droplets of all diameters enter the through-tool channel, but for both channels, very few large droplets reach the outlet of the channel. Larger droplets can hardly be carried along with the primary phase because of their high momentum and end up impacting the wall. Even though these droplets have a high velocity, the component of their velocity normal to the wall surface is comparatively small. Because of this, most of these droplets fall in the spreading zone, while some fall in the splashing zone based on the wall film model (Sec. 3.2). Once the droplets stick to the wall and form a lubricant film, their velocity reduces, and it takes much longer for the fluid film to reach the channel outlet. The instantaneous image can only provide information about the current location of the droplets and does not provide any information about the droplets that have already exited the control volume. To look at the number of droplets that have already exited the control volume, a histogram of the mass distribution of the droplets crossing the outlet boundary is shown in Fig. 10. It can be clearly seen that a negligible number of larger droplets exit the control volume. An interesting difference between the triangular and circular channels is that the triangular channel can carry a larger portion of 1 μm droplets as compared to the circular channel, but the circular channel can carry a higher mass of droplets of 2 μm diameter. Nonetheless, for both cases, over 95% (volume fraction) of the lubricant droplets end up sticking to the wall.

4.2 Cutting Region

4.2.1 Primary Flow. Figure 11 shows the velocity streamlines of the primary phase for all cases. Figures 11(*a*) and 11(*b*) show the velocity streamlines for the circular channel drill without and with a gash. It can be clearly seen that a gash increases the velocity of the fluid in the local region directly underneath it. However, no improvement is seen near the cutting edge with the implementation of the gash. A similar trend is seen for the triangular channel as shown in Figs. 11(*c*) and 11(*d*), where the local velocity directly below the gash increases, but no improvement in penetration to the cutting edge is seen. For both cases, the inclusion of a gash provided a 10% increase in the mass flowrate. The increase is subtle but might help improve the heat transfer capability of the fluid. For all cases, a fluid dead zone is observed near the outermost part of the cutting. This region has the highest cutting velocity and requires the most amount of cooling, but practically no flow can reach there. This might be a reason why high tool wear is observed near the drill margin.

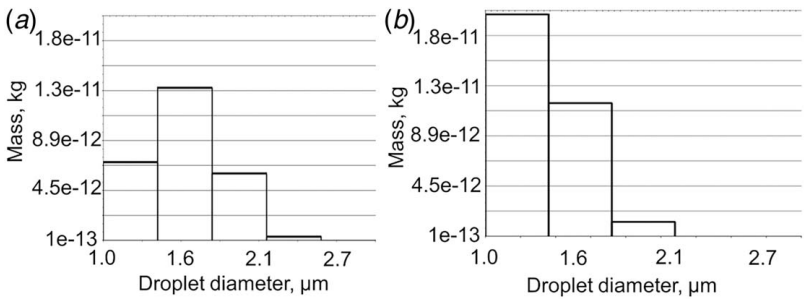

Fig. 10 Droplet size distribution at the outlet: (*a*) circular channel and (*b*) triangular channel

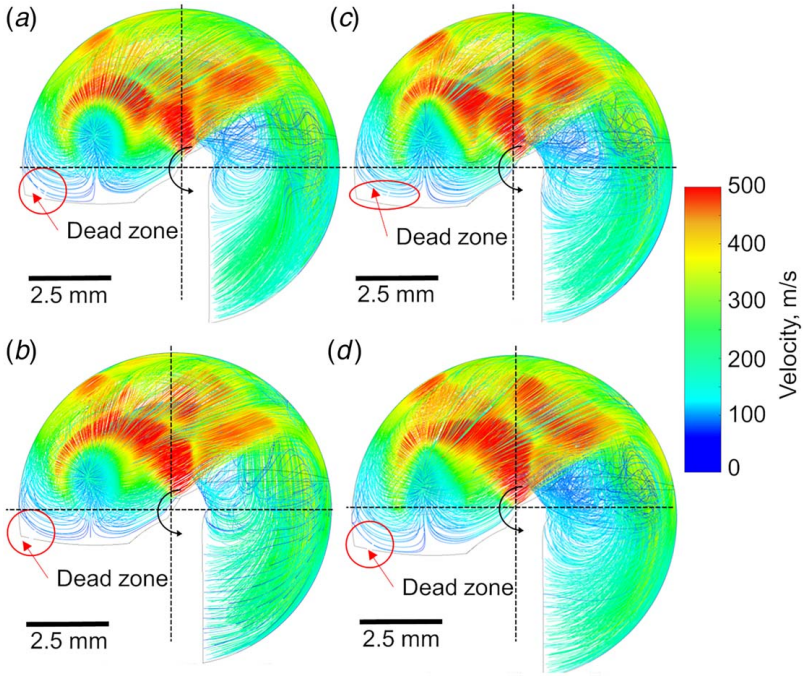

Fig. 11 Primary phase velocity streamlines bottom view: (*a*) circular channel without gash, (*b*) circular channel with gash, (c) triangular channel without gash, and (*d*) triangular channel with gash

4.2.2 Secondary Flow. Unlike the previous section, where volume fraction is used to show the distribution of the secondary phase, this section uses the lubricant film thickness at the hole bottom at 0.005 s, which is at the end of the simulation, to compare among cases. This was done because the volume fraction only shows the surface data, while the lubricant film thickness can also provide insight into the thickness of the lubricant film formed. This is more representative of the friction reduction capacity of the fluid. FLUENT can calculate the lubricant film thickness by solving the conservation of mass equation for the droplet mass that has adhered to the wall.

Figure 12 shows the result of the lubricant film formed at the hole bottom when the droplets exiting the through-tool channel are transferred to the inlet of the cutting region. Since the modeled time is only 0.005 s, the fluid film formed is very thin. This film is expected to grow as time progresses, but no change in the relative shape is expected. It can be noted from all the figures that the lubricant cannot reach the cutting edge of the tool. As can be seen by comparing Figs. 12(*a*) and 12(*b*), no improvement is observed in the lubricant penetration to the cutting edge with the inclusion of a gash. A similar trend is observed for the triangular channel, as seen in Figs. 12(*c*) and 12(*d*).

Although the droplets can be transferred from the through-tool channel control volume to the cutting region control volume, the lubricant mass exiting the through-tool channel outlet is a small fraction of what entered (less than 5%). A big portion of droplets end up sticking to the wall surface, and they travel very slowly compared to the bulk of the fluid, as explained in Sec. 4.1.2. These droplets can eventually exit the through-tool channel but will require a long flow time to be modeled. Moreover, the droplet breakup from the lubricant film into the bulk of the fluid due to Taylor's instabilities is not included in the model. Therefore, to independently investigate the effect of the cutting region geometry as well as to uncouple the effect of droplet distribution in the

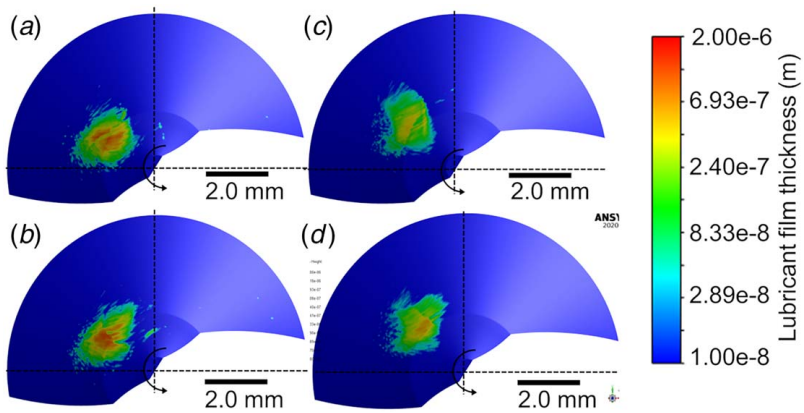

Fig. 12 Lubricant film thickness on hole bottom with droplet transferred from through-tool channel to the cutting region: (*a*) circular channel without gash, (*b*) circular channel with gash, (c) triangular channel without gash, and (*d*) triangular channel with gash

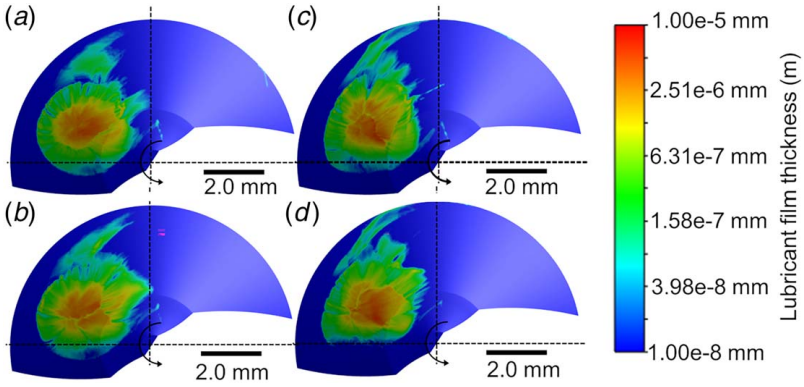

Fig. 13 Lubricant film thickness on hole bottom with uniform droplet distribution: (*a*) circular channel without gash, (*b*) circular channel with gash, (*c*) triangular channel without gash, and (*d*) triangular channel with gash

through-tool channel region, droplets with a size distribution shown in Fig. 6 were inserted uniformly across the inlet section of the cutting region control volume. The new results of all cases are shown in Fig. 13.

Comparing Figs. 13(*a*) and 13(*b*), the lubricant coverage spreads farther in the direction away from the cutting edge with the implementation of the gash. Yet, gash does not help the flow penetrate into the cutting edge. A similar phenomenon in the triangular channel is observed (Figs. 13(*c*) and 13(*d*)). However, there is a noticeable difference in the lubricant coverage between the circular channel and the triangular channel. The triangular channel provides a more uniform coverage across the area as compared to the circular channel. However, the penetration of the lubricant is lower. Contrastingly, for the circular channel, the lubricant penetration is high but only near the center of the cutting edge.

In summary, in the cutting region, the CFD results showed the influence of gash and through-tool channel shape to some extent. The velocity streamlines for the primary phase show that the velocity near the cutting edge is very low. The gap between the tool and the hole bottom is extremely small for the fluid to penetrate into the cutting edge. For all the cases, the region near the outermost portion of the cutting edge has the least fluid flow. That region is constrained from three sides, and therefore flow stagnation is observed. The gash increases the total fluid flowrate and can be beneficial for providing more cooling. Although a gash does not directly improve the fluid penetration to the cutting edge, it directs the fluid toward the chip generated by the second cutting edge. This may help in cooling the chip and reducing the heat conduction to the tool. It also directs the lubricant onto the hole wall, which may help in reducing the friction between the margin of the drill and the hole wall.

The fluid film thickness results for all the cases also show dependence on the through-tool channel shape and the gash. The region closest to the cutting edge has the deepest fluid penetration. For the circular channel, the lubricant film reaches the fastest to a narrow portion of the cutting edge which is about halfway from the center of the drill. While for the triangular channel, the fluid spreads more evenly across the central portion of the cutting edge.

5 Experimental Observation

5.1 Experimental Setup. As mentioned in the Introduction section, in-situ visualization of drilling is extremely difficult due to the lack of optical access to the drilling zone. It is also not possible to acquire commercial drilling tools with an identical drill point but different channel shapes and gashes for a controlled experiment. Therefore, a drilling testbed was specifically designed and fabricated for this purpose. The method uses a transparent workpiece with cutting behavior similar to that of a ductile metal which allows optical access to the cutting zone while also replicating the active cutting process.

The experimental setup used to perform the cutting is shown in Fig. 14. The setup consists of a high-speed camera, light sources, a spindle with a dual-channel UNIST Infinity MQL system, and a moving platform to feed the workpiece in and out of the drill. The drill designs shown in Fig. 2 were 3D printed using Formlabs Form 3 (Cambridge, MA) SLA 3D printer with 25–50 μm resolution. This was done since it allowed freedom in the design of the drill irrespective of its commercial availability. The material used must be clear, easily cut by the 3D printed drills, and can form proper chips like ductile materials. Glycerin was found to be the best choice for the workpiece material. Figure 14(*b*) shows the glycerin workpiece used for the experiments, and Fig. 14(*c*) confirms its wettability (18–22 deg contact angle), similar to that of actual metals. The chip formed while machining glycerin is shown in Fig. 14(*d*), containing curled and continuous chips.

5.2 Experimental Results. Drilling tests were performed on a glycerin workpiece, and the cutting was observed from the bottom view, as shown in Fig. 15. The drill was rotating at 500 rpm, and the feed was 0.2 mm/rev. The contact between the cutting edge and the workpiece shows a dark black edge, and the relative location of the through-tool channel exit is highlighted in the figure. The formation of the chip can be observed in front of the cutting edge. The formation of lubricant film on the hole bottom can be clearly observed in the continuous video. In this particular frame, no fluid penetration

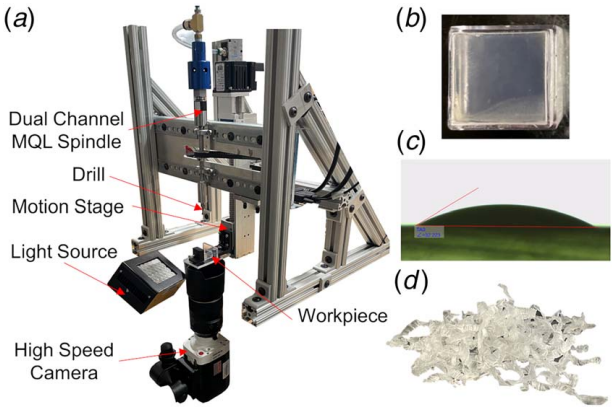

Fig. 14 (*a*) Experimental setup to replicate dual channel MQL spindle and drill glycerin, (*b*) glycerin workpiece used for the experiments, (*c*) contact angle of the lubricant with glycerin, and (*d*) chips formed while machining of glycerin

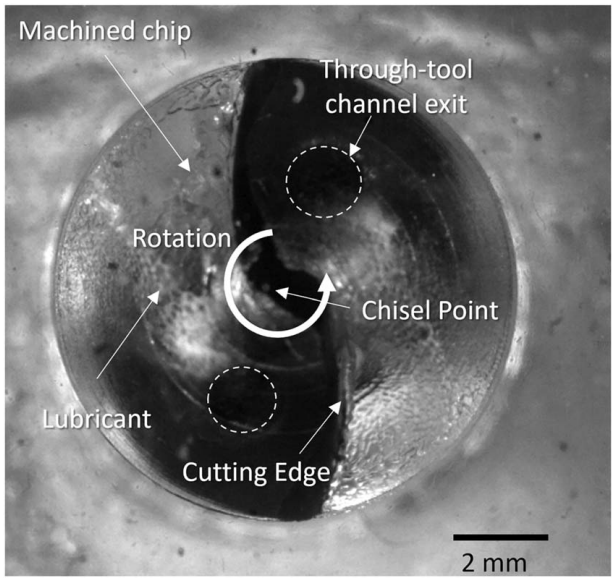

Fig. 15 Bottom view of drilling glycerin and identification of the features of the flow

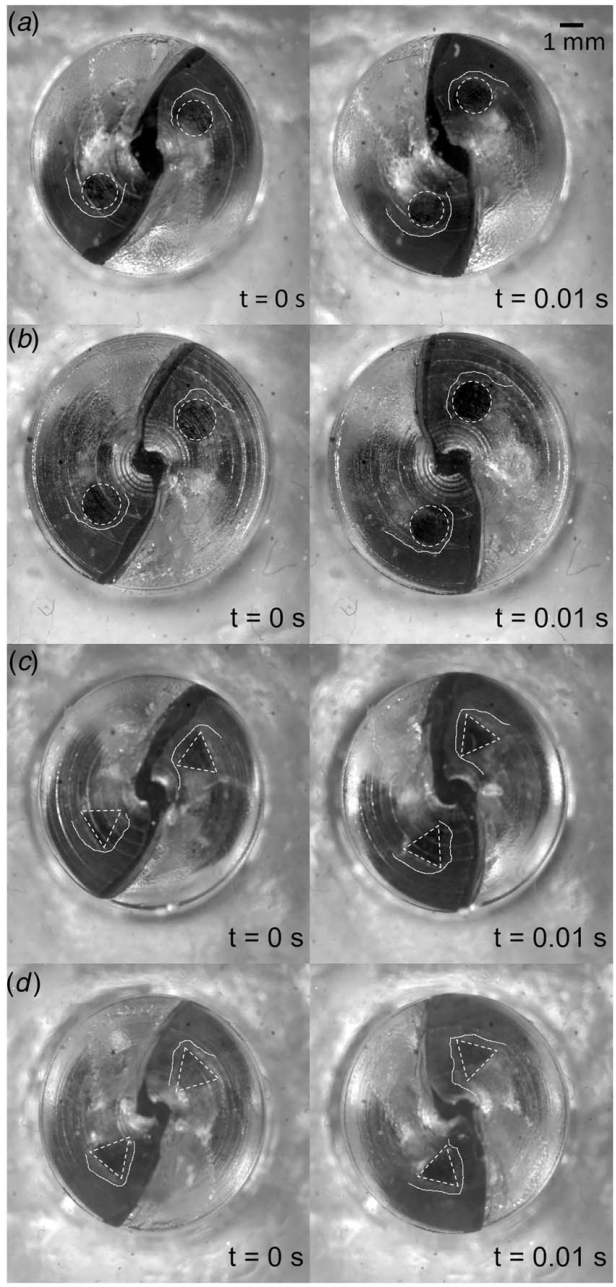

Fig. 16 Bottom view of in-situ drilling at different instants: (*a*) circular channel without gash, (*b*) circular channel with gash, (*c*) triangular channel without gash, and (*d*) triangular channel with gash

can be seen toward the cutting edge. Most of the lubricant flows away from the cutting edge and is directed toward the margin of the other cutting edge. This observation coincides with the overall CFD results in Figs. 11–13.

The results for all the cases are shown in Fig. 16. The views at different time frames are shown for each case. It can be confirmed that in all cases, the lubricant does not penetrate into the cutting region. Most of the lubricant is directed away from the cutting edge towards the margin of the second cutting edge. A thin film of lubricant spreads radially outwards from the exit of the through-tool channel. An increase in the velocity of the lubricant near the gash region is also observed. This phenomenon matches with the CFD results, where the primary phase velocity increases with the inclusion of a gash. Additionally, the general distribution of the lubricant obtained for all the cases matches well with the lubricant film thickness predicted by the CFD model. The CFD model shows slightly deeper penetration of the lubricant towards the cutting edge. This may be explained by the larger contact angle of the lubricant with glycerin as compared to aluminum which can reduce the spreading of the lubricant.

6 Discussion

From the results, the through-tool channel shape affects the lubricant droplet distribution. The droplets are subject to three types of forces, namely, drag, centrifugal, and Coriolis. The density of the lubricant is a few orders of magnitudes higher than that of the primary phase, and therefore, the droplets have a greater influence by the centrifugal and Coriolis force. Based on the results, only smaller droplets of 1–1.5 μm exit the channel as droplets; the larger droplets fail to follow the primary flow and end up sticking to the wall. This is reasonable because doubling the diameter of the droplets increases the mass of the droplets by eight times, which considerably increases the centrifugal force. Furthermore, the lubricant used has a high surface energy and low surface tension; therefore, it tends to readily stick to the channel wall and fails to re-enter the bulk of the fluid. Once the fluid film thickness increases beyond a certain extent, the shear force from the primary phase can generate Kevin–Helmholtz instability and break the fluid film surface to form droplets. However, this was not modeled in the current study using a Lagrangian DPM. Yet, this is an important phenomenon found to guide the future development of simulation work. The effect of drill rotation speed is not particularly studied in the paper, but it is expected that with an increase in the rotation speed, the centrifugal and Coriolis forces will become stronger, thus reducing the flowrate and droplets penetration.

Although many physics-based and empirical models have been incorporated into this model, certain assumptions must be made to facilitate the simulation process, which also limits the number of phenomena that can be concluded from the model. First, the model does not include any droplet-droplet collisions, and therefore high droplet volume fraction regions cannot be fully modeled. This is particularly true in the near-wall regions where the formation of fluid film is unavoidable. The model also does not include the effect of capillary action. Capillary action is important for fluid penetration into the cutting edge as it deposits on the hole bottom. To be able to include both these phenomena, either a complete multiphase

model or an Eulerian formulation of the fluid film is needed. Both are possible but will increase the computational load, which disobeys the objective of this study to use a more efficient model to approximate droplet dynamics in the MQL flow. Nonetheless, as seen from the experiments, the lubricant cannot reach the cutting edge even in the presence of the capillary force due to the motion of the bottom surface. The hole bottom moves away from the cutting edge and therefore does not provide enough time for the capillary action to penetrate the lubricant to the cutting edge. Lastly, even though the current model does not completely capture all the aspects of MQL flow, it still provides useful insights into the effect of channel geometry and the drill geometry on MQL flow which was verified by the experimental validation. All phenomena concluded can also be justified either through the literature data or known physics.

7 Conclusion

An Euler–Lagrange CFD model was applied to simulate lubricant droplets in through-tool MQL drilling to provide a better understanding of various tool designs. The results from the CFD were validated using a novel in-situ high-speed imaging technique developed. The in-situ technique provided optical access to the cutting zone while maintaining the active cutting operation and rotation of the drill. Two channel geometries and two gashing conditions were compared to investigate their effects on the lubricant coverage in the cutting zone. The major findings are concluded as follows. First, the centrifugal and Coriolis forces generated due to the rotation of the drill were significant enough to generate a secondary flow in the channel, which affected the droplet distribution to some degree. Second, the primary phase was incapable of conveying the larger droplets effectively through the channel due to the high Stokes number, because of which they ended up impacting the channel wall and forming a fluid film. Therefore, the actual flow at the drill bit outlet (before entering the cutting region) is likely a result of the second atomization at the channel exit. Smaller droplets ($<2\ \mu$m) can be easily carried by the primary phase through the channel to the cutting zone. Third, the channel geometry (circular versus triangular) has limited effects on the lubricant coverage, despite having a gash to create a larger flow stream. The cutting edges and drill margin can hardly be reached by the lubricant droplets, which may explain the higher tool wear in those regions in MQL deep-hole drilling.

Lastly, it should be emphasized that several assumptions were made in this work (as mentioned in the Discussion section) that limit the CFD model in simulating certain phenomena. However, although the coverage of the fluid film cannot be quantified nor validated precisely, the model provides information in a qualitative manner to explain how the droplet size, channel geometry, and drill point design may lead to various outcomes.

Acknowledgment

The authors would like to thank National Science Foundation (NSF) for providing financial support for the research through grant #1760985, and Dr. Dorrin Jarrahbashi for her feedback on the CFD model.

Conflict of Interest

There are no conflicts of interest.

Data Availability Statement

The datasets generated and supporting the findings of this article are obtainable from the corresponding author upon reasonable request.

Nomenclature

k = kinetic energy of the fluid
E = impact energy of the droplet
$\mathbf{r}$ = radial vector
$\mathbf{V}$ = velocity vector for air
d_d = droplet diameter
g_i = component of gravity in ith direction
h_o = preexistent fluid film thickness
y_s = mass fraction splashing from the surface
C_D = coefficient of drag for the droplets
E_{crit} = critical impact energy for the droplets
F_D = drag force
V_{di} = component of droplet velocity in ith direction
$V_{d,x}$ = velocity component of droplet in X direction
$V_{d,y}$ = velocity component of droplet in Y direction
V_n = velocity of the droplet in normal direction to the impact surface
V_y = velocity component of air in Y direction
V_x = velocity component of air in X direction
$\mathbf{v}_r$ = radial component of velocity
$\mathbf{F}_g$ = gravitational force
$\mathbf{V}_i$ = component of air velocity in ith direction
Re = Reynolds number
δ_{bl} = boundary layer thickness
∇p = pressure gradient
ε = rate of dissipation of kinetic energy
μ = viscosity of droplets
ρ_a = density of air
ρ_d = density of droplets
$\underline{\sigma}$ = surface tension
$\underline{\tau}$ = stress tensor
ω = specific rate of dissipation
Ω = angular velocity of the control volume
$\mathbf{\Omega}$ = rotation vector

References

[1] Filipovic, A., and Stephenson, D. A., 2006, "Minimum Quantity Lubrication (MQL) Applications in Automotive Power-Train Machining," Mach. Sci. Technol., **10**(1), pp. 3–22.
[2] Stephenson, D. A., and Agapiou, J. S., 2018, *Metal Cutting Theory and Practice*, CRC Press.
[3] Sharma, V. S., Singh, G., and Sørby, K., 2015, "A Review on Minimum Quantity Lubrication for Machining Processes," Mater. Manuf. Processes, **30**(8), pp. 935–953.
[4] Raval, J. K., Stephenson, D. A., and Tai, B. L., 2020, "Effect of Oil Flow Rate on Production Through-Tool Dual Channel MQL Drilling," ASME 2020 15th International Manufacturing Science and Engineering Conference, Virtual Online, Sept. 3, p. V001T05A007, ASME.
[5] Masoudi, S., Vafadar, A., Hadad, M., Jafarian, F., 2018, "Experimental Investigation Into the Effects of Nozzle Position, Workpiece Hardness, and Tool Type in MQL Turning of AISI 1045 Steel," Mater. Manuf. Processes, **33**(9), pp. 1011–1019.
[6] Amiril, S., Rahim, E., and Hishamudin, A., 2019, "Effect of Nozzle Distance and Cutting Parameters on MQL Machining of AISI 1045," J. Phys.: Conf. Ser., **1150**(1), pp. 012–045.
[7] Duchosal, A., Leroy, R., Vecellio, L., Louste, C., Ranganathan, N., 2013, "An Experimental Investigation on Oil Mist Characterization Used in MQL Milling Process," Int. J. Adv. Manuf. Technol., **66**(5), pp. 1003–1014.
[8] Nam, J. S., Lee, P.-H., and Lee, S. W., 2011, "Experimental Characterization of Micro-Drilling Process Using Nanofluid Minimum Quantity Lubrication," Int. J. Mach. Tools Manuf., **51**(7–8), pp. 649–652.
[9] Pei, H. J., Shen, C. G., Zheng, W. J., and Wang, G. C., 2010, "CFD Analysis and Experimental Investigation of Jet Orientation in MQL Machining," Adv. Mater. Res., **135**, pp. 462–466.
[10] Balan, A. S. S., Kullarwar, T., Vijayaraghavan, L., Krishnamurthy, R., 2017, "Computational Fluid Dynamics Analysis of MQL Spray Parameters and Its Influence on Superalloy Grinding," Mach. Sci. Technol., **21**(4), pp. 603–616.
[11] Dean, W. R., 1927, "XVI. Note on the Motion of Fluid in a Curved Pipe," Lond. Edinb. Dublin Philos. Mag. J. Sci., **4**(20), pp. 208–223.
[12] Germano, M., 1989, "The Dean Equations Extended to a Helical Pipe Flow," J. Fluid Mech., **203**, pp. 289–305.
[13] Yamamoto, K., Wu, X., Nozaki, K., Hayamizu, Y., 2006, "Visualization of Taylor–Dean Flow in a Curved Duct of Square Cross-Section," Fluid Dyn. Res., **38**(1), p. 1.
[14] Yamamoto, K., Yanase, S., and Yoshida, T., 1994, "Torsion Effect on the Flow in a Helical Pipe," Fluid Dyn. Res., **14**(5), p. 259.

[15] Oezkaya, E., Beer, N., and Biermann, D., 2016, "Experimental Studies and CFD Simulation of the Internal Cooling Conditions When Drilling Inconel 718," Int. J. Mach. Tools Manuf., **108**, pp. 52–65.
[16] Johns, A., Merson, E., Royer, R., Thompson, H., and Summers, J., 2018, "A Numerical Investigation of Through-Tool Coolant Wetting Behaviour in Twist-Drilling," J. Fluid Flow Heat Mass Transfer, **5**, pp. 44–52.
[17] Falcone, M., Buss, L., and Fritsching, U., 2022, "Eulerian–Lagrangian–Eulerian Simulations of Two-Phase Minimum Quantity Lubrication Flow in Internal Drill Bit Channels," Processes, **10**(3), p. 600.
[18] Shao, Y., Adetoro, O. B., and Cheng, K., 2020, "Development of Multiscale Multiphysics-Based Modelling and Simulations With the Application to Precision Machining of Aerofoil Structures," Eng. Comput., **38**(3), pp. 1330–1349.
[19] Park, K.-H., Olortegui-Yume, J. A., Yoon, M.-C., Kwon, P., 2010, "A Study on Droplets and Their Distribution for Minimum Quantity Lubrication (MQL)," Int. J. Mach. Tools Manuf., **50**(9), pp. 824–833.
[20] Park, K.-H., Olortegui-Yume, J. A., Joshi, S., Kwon, P., Yoon, M.-C., Lee, G.-B., and Park, S.-B., 2008, "Measurement of Droplet Size and Distribution for Minimum Quantity Lubrication (MQL)," 2008 International Conference on Smart Manufacturing Application, Goyangi, South Korea, Apr. 9–11, IEEE.
[21] Dasch, J. M., and Kurgin, S. K., 2010, "A Characterization of Mist Generated From Minimum Quantity Lubrication (MQL) Compared to Wet Machining," Int. J. Mach. Mach. Mater., **7**(1–2), pp. 82–95.
[22] Fluent, A., 2011, *Ansys Fluent Theory Guide*, 15317, Ansys Inc., USA, pp. 724–746.
[23] Stephenson, D. A., Hughey, E., and Hasham, A. A., 2019, "Air Flow and Chip Removal in Minimum Quantity Lubrication Drilling," Procedia Manuf., **34**, pp. 335–342.
[24] Johns, A. S., 2015, "Computational Fluid Dynamic Modelling and Optimisation of Internal Twist-Drill Coolant Channel Flow," Ph.D. dissertation, University of Leeds, Leeds, UK.
[25] Fallenstein, F., and Aurich, J., 2014, "CFD Based Investigation on Internal Cooling of Twist Drills," Procedia CIRP, **14**, pp. 293–298.
[26] Tai, B. L., Dasch, J. M., and Shih, A. J., 2011, "Evaluation and Comparison of Lubricant Properties in Minimum Quantity Lubrication Machining," Mach. Sci. Technol., **15**(4), pp. 376–391.
[27] Clift, R., Grace, J. R., and Weber, M. E., 2005, *Bubbles, Drops, and Particles*, Dover Publications Inc., Mineola, NY.
[28] Stanton, D. W., and Rutland, C. J., 1996, "Modeling Fuel Film Formation and Wall Interaction in Diesel Engines," J. Engines, **105**, pp. 808–824.
[29] Naber, J., and Reitz, R. D., 1988, "Modeling Engine Spray/Wall Impingement," J. Engines, **97**, Sec. 6, pp. 118–140.
[30] Mundo, C., Sommerfeld, M., and Tropea, C., 1995, "Droplet-Wall Collisions: Experimental Studies of the Deformation and Breakup Process," Int. J. Multiphase Flow, **21**(2), pp. 151–173.
[31] Iskandar, Y., et al., 2014, "Flow Visualization and Characterization for Optimized MQL Machining of Composites," CIRP Ann., **63**(1), pp. 77–80.
[32] Dasch, J., et al., 2005, "Characterization of Fine Particles From Machining in Automotive Plants," J. Occup. Environ. Hyg., **2**(12), pp. 609–625.
[33] Raval, J. K., and Tai, B. L., 2021, "An Optical Tomographic Method to Characterize the Mist Distribution in MQL Tools," J. Manuf. Process., **62**, pp. 275–282.